Inorganic Chemistry

Article

pubs.acs.org/IC

Insight into the Reactivity and Electronic Structure of Dinuclear Dinitrosyl Iron Complexes

Feng-Chun Lo,[†] Ya-Wen Li,[‡] I-Jui Hsu,*[,‡] Chien-Hong Chen,*[,§,∥] and Wen-Feng Liaw[†]

[†]Department of Chemistry, National Tsing Hua University, Hsinchu 30013, Taiwan
[‡]Department of Molecular Science and Engineering, National Taipei University of Technology, Taipei 10608, Taiwan
[§]School of Medical Applied Chemistry, Chung Shan Medical University, Taichung 40201, Taiwan
[∥]Department of Medical Education, Chung Shan Medical University Hospital, Taichung 40201, Taiwan

Supporting Information

ABSTRACT: A combination of N/S/Fe K-edge X-ray absorption spectroscopy (XAS), X-ray diffraction data, and density functional theory (DFT) calculations provides an efficient way to unambiguously delineate the electronic structures and bonding characters of Fe−S, N−O, and Fe−N bonds among the direduced-form Roussin's red ester (RRE) $[Fe_2(\mu\text{-}SPh)_2(NO)_4]^{2-}$(**1**) with $\{Fe(NO)_2\}^{10}$-$\{Fe(NO)_2\}^{10}$ core, the reduced-form RRE $[Fe_2(\mu\text{-}SPh)_2(NO)_4]^{-}$(**3**) with $\{Fe(NO)_2\}^{9}$-$\{Fe(NO)_2\}^{10}$ core, and RRE $[Fe_2(\mu\text{-}SPh)_2(NO)_4]$ (**4**) with $\{Fe(NO)_2\}^{9}$-$\{Fe(NO)_2\}^{9}$ core. The major contributions of highest occupied molecular orbital (HOMO) $113\alpha/\beta$ in complex **1** is related to the antibonding character between Fe(d) and Fe(d), Fe(d), and S atoms, and bonding character between Fe(d) and NO(π^*). The effective nuclear charge (Z_{eff}) of Fe site can be increased by removing electrons from HOMO to shorten the distances of Fe⋯Fe and Fe−S from **1** to **3** to **4** or, in contrast, to increase the Fe−N bond lengths from **1** to **3** to **4**. The higher IR ν_{NO} stretching frequencies (1761, 1720 cm^{-1} (**4**), 1680, 1665 cm^{-1} (**3**), and 1646, 1611, 1603 cm^{-1} (**1**)) associated with the higher transition energy of $N_{1s} \rightarrow \sigma^*(NO)$ (412.6 eV (**4**), 412.3 eV (**3**), and 412.2 eV (**1**)) and the higher Z_{eff} of Fe derived from the transition energy of $Fe_{1s} \rightarrow Fe_{3d}$ (7113.8 eV (**4**), 7113.5 eV (**3**), and 7113.3 eV (**1**)) indicate that the N−O bond distances of these complexes are in the order of **1** > **3** > **4**. The N/S/Fe K-edge XAS spectra as well as DFT computations reveal the reduction of complex **4** yielding complex **3** occurs at Fe, S, and NO; in contrast, reduction mainly occurs at Fe site from complex **3** to complex **1**.

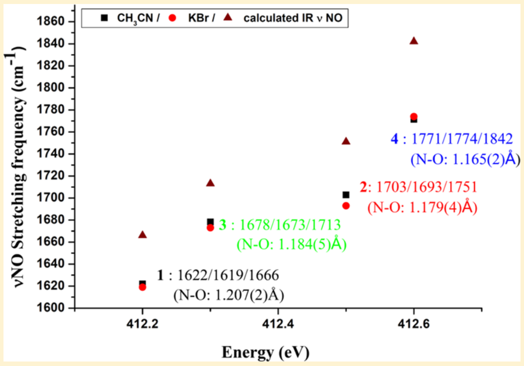

■ INTRODUCTION

Nitric oxide (NO), a ubiquitous endocrine molecule, has been intensively studied because of its physiological functions such as smooth muscle relaxation,[1−3] neurotransmission,[4] immune response,[5] and blood pressure.[6] Dinitrosyl iron complexes (DNICs), the endogenous NO-derived species as S-nitrosothiols (RSNO), are thought to serve as storage and carriers of NO in biological system.[7−10] *In vivo*, the naturally occurring DNICs are classified into protein-bound DNICs and low-molecular-weight DNICs (LMW-DNICs). Protein-bound DNICs derived from NO-mediated degradation of [Fe−S] cluster-containing proteins are considered as the storage of NO or $\{Fe(NO)_2\}$ moiety, and LMW-DNICs produced via the displacement of protein-bound DNICs with free thiols/thiolates may serve as the donor of NO or $\{Fe(NO)_2\}$ moiety.[11−14] Biologically, both protein-bound DNICs and LMW-DNICs are characterized by their distinctive electron paramagnetic resonance (EPR) signals at $g = 2.03$.[15,16] In spite of the major thiol components of cellular DNICs composed of cysteinate residues in proteins and mobile units such as glutathione,[17−20] the DNICs ligated by histidine, deprotonated imidazole, and tyrosinate were found and proposed in enzymology based on EPR spectra.[11,17,19,21−24] Recently, the crystal structure of human glutathione S-transferase (GST) P1−1-bound dinitrosyldiglutathionyl iron complex (GSH-DNIC) ligated with tyrosinate and glutathione has been determined.[17] In inorganic chemistry, DNICs can be classified into the paramagnetic, oxidized form DNICs ($\{Fe(NO)_2\}^9$ DNICs) and the diamagnetic, reduced-form DNICs ($\{Fe(NO)_2\}^{10}$ DNICs), based on the oxidation levels of the $Fe(NO)_2$ unit. Up to now, numbers of oxidized and reduced LMW-DNICs containing various ligation modes were synthesized for the spectroscopic references and the study of potential NO delivery.[25−32]

In addition to DNICs, Roussin's red esters (RREs), the dimeric form of DNICs considered to act the similar role as DNICs, were also observed upon nitrosylation of various [Fe−S] protein and Fe-containing proteins. For example, nitrosylation of a Rieske-type ToMOC protein containing a [2Fe−

Received: May 5, 2014
Published: October 3, 2014

Chart 1

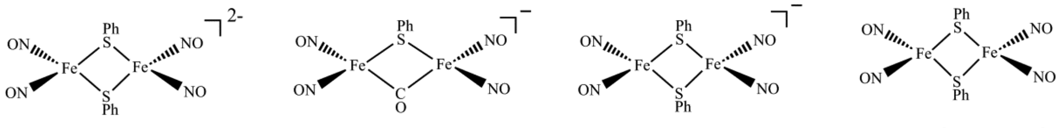

$\{Fe(NO)_2\}^{10}$-$\{Fe(NO)_2\}^{10}$ (1)

$\{Fe(NO)_2\}^{10}$-$\{Fe(NO)_2\}^{10}$ (2)

$\{Fe(NO)_2\}^{10}$-$\{Fe(NO)_2\}^{9}$ (3)

$\{Fe(NO)_2\}^{9}$-$\{Fe(NO)_2\}^{9}$ (4)

Scheme 1

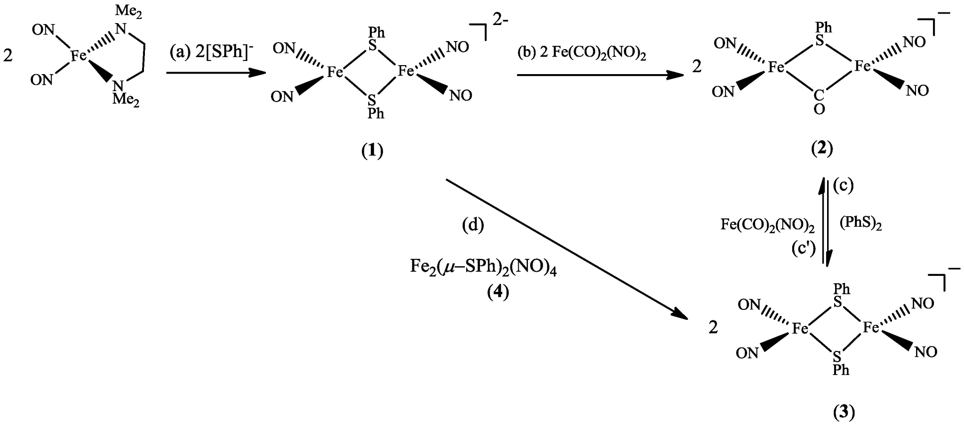

2S] cluster resulting in the formation of protein-bound RRE was reported.[33] The [4Fe−4S] cluster was nitrosylated to convert into protein-bound RRE when WhiB-like protein was treated with NO.[34] Furthermore, the formation of protein-bound RREs and DNICs with 4:1 molar ratio was reported upon treatment of the [4Fe−4S] fumarate and nitrate reductase regulator (FNR) protein with NO, based on UV−vis and EPR spectra.[35,36] Unlike DNICs identified by its characteristic EPR signal at g_{av} =2.03, RREs are more difficult to identify biologically due to their EPR silence. In chemistry, DNICs exist in reversible interconversion with RREs, regulated by concentration, solvent polarity, and the nature of the thiolate ligand.[37] In addition to the neutral $\{Fe(NO)_2\}^9$-$\{Fe(NO)_2\}^9$ RREs, $\{Fe(NO)_2\}^9$-$\{Fe(NO)_2\}^{10}$ reduced RREs have been prepared and identified.[37−39] EPR spectra of the reduced RREs, resulting from chemical reduction of the corresponding RREs, are identical to those obtained from reduction of DNICs derived from nitrosylation of aconitase and HiPIP-containing protein-bound DNIC.[38] Recently, the dinuclear DNICs with $\{Fe(NO)_2\}^{10}$-$\{Fe(NO)_2\}^{10}$ core (direduced RREs) were synthesized via the chemical reduction of the corresponding anionic $\{Fe(NO)_2\}^9$ DNICs.[40] According to the oxidation levels and configurations of the $\{Fe(NO)_2\}$-$\{Fe(NO)_2\}$ core of dinuclear DNICs, these dinuclear DNICs could be classified into: (i) the EPR-silent $\{Fe(NO)_2\}^9$-$\{Fe(NO)_2\}^9$ species with sulfide-bridged ligands/mixed sulfide−thiolate-bridged ligands/thiolate-bridged ligands, (ii) the EPR-active $\{Fe(NO)_2\}^9$-$\{Fe(NO)_2\}^9$ species with two separated $\{Fe(NO)_2\}^9$ moieties, (iii) the EPR-active $\{Fe(NO)_2\}^9$-$\{Fe(NO)_2\}^{10}$ species, and (iv) the EPR-silent $\{Fe(NO)_2\}^{10}$-$\{Fe(NO)_2\}^{10}$ species with mixed carbonyl−thiolate-bridged ligands/thiolate-bridged ligands.[25,40,41]

In addition to EPR spectroscopy, the nuclear resonance vibrational spectroscopy (NRVS) has been applied to determine the formation of DNICs and RREs according to their characteristic vibrational frequencies.[42] Furthermore, the characteristic pre-edge peak energy in Fe K-edge absorption spectra, ranging from 7113.1 to 7113.3 eV for the mononuclear $\{Fe(NO)_2\}^{10}$ DNICs/dinuclear $\{Fe(NO)_2\}^{10}$-$\{Fe(NO)_2\}^{10}$ DNICs, from 7113.6 to 7113.8 eV for the dinuclear $\{Fe(NO)_2\}^9$-$\{Fe(NO)_2\}^9$ DNICs, and from 7113.4 to 7113.8 eV for the mononuclear $\{Fe(NO)_2\}^9$ DNICs, are adopted to probe the various DNICs.[28,40] In particular, the distinct pre-edge absorption energy and pattern of S K-edge absorption spectra were also utilized to distinguish the mononuclear and dinuclear DNICs with bridging-sulfide and bridging-thiolate ligands.[40,43]

In this study, the $\{Fe(NO)_2\}^{10}$-$\{Fe(NO)_2\}^{10}$ direduced-form RRE $[Fe_2(\mu\text{-SPh})_2(NO)_4]^{2-}$ (**1**), mixed-carbonyl−thiolate-bridged $\{Fe(NO)_2\}^{10}$-$\{Fe(NO)_2\}^{10}$ direduced-form RRE $[Fe_2(\mu\text{-SPh})(\mu\text{-CO})(NO)_4]^-$ (**2**), $\{Fe(NO)_2\}^9$-$\{Fe(NO)_2\}^{10}$ reduced-form RRE $[Fe_2(\mu\text{-SPh})_2(NO)_4]^-$ (**3**), and $\{Fe(NO)_2\}^9$-$\{Fe(NO)_2\}^9$ RRE $[Fe_2(\mu\text{-SPh})_2(NO)_4]$ (**4**) were isolated and characterized as shown in Chart 1. The transformations among these dinuclear DNICs were unraveled. N/S/Fe K-edge XAS spectra and DFT computation employed to delineate the bonding character of Fe−S, N−O, and Fe−N bonds and Z_{eff} of Fe of the reversible redox-form RREs (RRE **4** ⇌ reduced RRE **3** ⇌ direduced RRE **1**) were demonstrated. Of importance, the correlations between IRν_{NO} stretching frequencies and $N_{1s} \rightarrow \sigma^*(NO)/N_{1s} \rightarrow \pi^*(NO)$ transition energies are uncovered.

RESULTS AND DISCUSSION

Synthesis of Dinuclear DNICs. As shown in Scheme 1a, the dinuclear DNIC $[PPh_4]_2[Fe_2(\mu\text{-SPh})_2(NO)_4]$ (**1**) was isolated as yellow-green solid (80% yield) by the treatment of $Fe(TMEDA)(NO)_2$ (TMEDA= *N,N,N′,N′*-tetramethylethylenediamine) with $[PPh_4][SPh]$ (1:1 molar ratio) in tetrahydrofuran (THF). Complex **1** displays extreme air sensitivity in CH_3CN/dimethyl sulfoxide solution, but is stable in solid state under nitrogen. The IR ν_{NO} spectrum of complex **1** shows stretching bands at 1646 (m), 1611 (s), and 1603 (s) cm^{-1} (KBr) (1644 (s) and 1604 (s) cm^{-1} (CH_3CN)), in accordance with the presence of the $\{Fe(NO)_2\}^{10}$ moiety. The slightly higher ν_{NO} stretching frequencies of complex **1**, compared with those of $[PPN]_2[Fe_2(\mu\text{-}S^tBu)_2(NO)_4]$,[40] are consistent with the distinct electronic effects of phenylthiolate and alkyl-thiolate ligands. The redox behavior of complex **1** was studied by cyclic voltammetry (CV) in CH_3CN with $[^nBu_4N][PF_6]$ as supporting electrolyte at ambient temperature. Complex **1** reveals two reversible oxidation−reduction processes at −0.79 and −1.41 V ($E_{1/2}$ vs Fc^+/Fc, scan rate of 0.5 V/s) (in Supporting Information (SI), Figure S1) corresponding to the $\{Fe(NO)_2\}^9$-$\{Fe(NO)_2\}^9$/$\{Fe(NO)_2\}^{10}$-$\{Fe(NO)_2\}^9$ couple and $\{Fe(NO)_2\}^{10}$-$\{Fe(NO)_2\}^9$/$\{Fe(NO)_2\}^{10}$-$\{Fe(NO)_2\}^{10}$ couple, respectively. The positive shift of reversible redox potential of complex **1**, compared with the analogous processes at −0.99 and −1.61 V ($E_{1/2}$ vs Fc^+/Fc) of $[PPN]_2[Fe_2(\mu\text{-}S^tBu)_2(NO)_4]$,[40] is a consequence of less electron density surrounding Fe of complex **1** and is consistent with the slightly higher ν_{NO} stretching frequencies of complex **1**.

When complex **1** was added to the THF solution of $[Fe(CO)_2(NO)_2]$ with a 1:2 stoichiometry at ambient temperature (Scheme 1b), a pronounced color change from orange to blue occurred. The transformation of the dinuclear DNIC **1** into $[PPh_4]_2[Fe_2(\mu\text{-}SPh)(\mu\text{-}CO)(NO)_4]$ (**2**) was observed and monitored with Fourier transform infrared (FTIR) spectroscopy. The IR ν_{NO} spectrum of complex **2** displays strong stretching bands at 1706 (s), 1694 (s) cm^{-1}, and one ν_{CO} stretching band at 1846 (w) cm^{-1} (THF). Presumably, the π-accepting labile CO of $\{Fe(NO)_2\}^{10}$ $[Fe(CO)_2(NO)_2]$ promoting the bridging-thiolate cleavage of $\{Fe(NO)_2\}^{10}$-$\{Fe(NO)_2\}^{10}$ complex **1** may rationalize the formation of complex **2** stabilized by π-accepting CO-bridging ligand. Upon addition of 1 equiv of $(PhS)_2$ to a THF solution of complex **2**, a pronounced color change from blue to dark green occurred under N_2 at ambient temperature. The shift in the IR ν_{NO} stretching frequencies from 1706 (s) and 1694 (s) cm^{-1} (THF) to 1688 (s) and 1667 (s) cm^{-1} (THF), comparable with those of dinuclear $\{Fe(NO)_2\}^{10}$-$\{Fe(NO)_2\}^9$ species,[37−39] was assigned to the formation of $\{Fe(NO)_2\}^{10}$-$\{Fe(NO)_2\}^9$ $[PPh_4][Fe_2(\mu\text{-}SPh)_2(NO)_4]$ (**3**), presumably derived from oxidative addition of $(PhS)_2$ into the $\{Fe(NO)_2\}^{10}$-$\{Fe(NO)_2\}^{10}$ core of complex **2**. Complex **3** exhibits an isotropic EPR signal at $g = 2.001$ at 298 K (SI, Figure S2), consistent with the g values of other analogous dinuclear $\{Fe(NO)_2\}^{10}$-$\{Fe(NO)_2\}^9$ species.[37−39] Reversibly, conversion of complex **3** into complex **2** was demonstrated by reaction of complex **3** with $[Fe(CO)_2(NO)_2]$ and monitored by IR ν_{NO} spectra (Scheme 1c′). The shift in the IR ν_{NO} stretching bands from 1688 (s) and 1667 (s) cm^{-1} (THF) to 1846 (w), 1814 (w), 1783 (s), 1757 (s), 1706 (s) and 1694 (s) cm^{-1} (THF) was assigned to the formation of complex **2** and dinuclear $\{Fe(NO)_2\}^9$-$\{Fe(NO)_2\}^9$ $[Fe_2(\mu\text{-}SPh)_2(NO)_4]$ (**4**). Isolation of the reaction mixture afforded complexes **2** and **4** in the yield of molar ratio 2:1. We also noticed that addition of complex **4** into complex **1** generates $\{Fe(NO)_2\}^{10}$-$\{Fe(NO)_2\}^9$ complex **3**, presumably, via intermolecular electron transfer from $\{Fe(NO)_2\}^{10}$-$\{Fe(NO)_2\}^{10}$ complex **1** to $\{Fe(NO)_2\}^9$-$\{Fe(NO)_2\}^9$ complex **4** (Scheme 1d). In contrast to the formation of anionic reduced RREs by reduction of neutral RREs or oxidation of direduced RREs, the transformation of complexes **1**/**2** to complex **3**, respectively, provides the new synthetic pathway for synthesis of anionic reduced RREs.

Similar to CO known to serve as a probe of the electron density at transition metal, the shift of the NO stretching frequencies also reflects the variation of the electron density at Fe atom of $\{Fe(NO)_2\}$ motif.[44] The IR ν_{NO} stretching bands at 1644 (m) and 1604 (s) cm^{-1} (CH_3CN) for complex **1**; 1688 (s) and 1671 (s) cm^{-1} (CH_3CN) for complex **3**; and 1817 (w), 1786 (s) and 1759 (s) cm^{-1} (CH_3CN) for complex **4** reveals that the electronic richness of Fe atoms in complexes **1**, **3**, and **4** is in the order of complex **1** > complex **3** > complex **4**. However, dinuclear $\{Fe(NO)_2\}^{10}$-$\{Fe(NO)_2\}^{10}$ complex **2** displays the IR ν_{NO} stretching frequencies at 1709 (s) and 1697 (s) cm^{-1} (CH_3CN), which is significantly higher than those of complex **1** and slightly higher than those of complex **3**. Obviously, the strong π-accepting bridging CO of complex **2** effectively relieves the electron density at Fe atom of $\{Fe(NO)_2\}^{10}$-$\{Fe(NO)_2\}^{10}$ complex **2**. The electronic richness of Fe atoms of complexes **1**−**4**, probed by the IR ν_{NO} stretching frequencies, reveals that the electronic richness of Fe atoms of complexes **1**−**4** is in the order of complex **1** > complex **3** > complex **2** > complex **4**.

Structure. Figures 1−3 display the thermal ellipsoid plots of complexes **1**−**3**, and selected bond distances and angles are given in the figure captions. Two nitrosyl groups and two bridging thiolates define the distorted tetrahedrlal geometry of each Fe atom in complexes **1** and **3**, while each Fe atom is connected to two nitrosyl groups, bridging thiolate and carbonyl, with a pseudotetrahedral geometry in complex **2**. The $[Fe(\mu\text{-}S)_2Fe]$ core geometries of complexes **1** and **3** are best described as a planar rhombus with two bridging-phenylthiolate ligands in the anticonformation; in the meantime, the $[Fe(\mu\text{-}S)(\mu\text{-}C)Fe]$ core geometry of complex **2** is best described as a butterfly-like structure with a dihedral angle of 172.23° (the intersection of the Fe_2S and Fe_2C planes), comparable to the dihedral angle of 170.1° in $[PPh_4]$-$[(NO)_2Fe(\mu\text{-}CO)(\mu\text{-}SC_6H_4\text{-}o\text{-}N(CH_3)_2)Fe(NO)_2]$.[25] The longer average Fe−N bond distance of 1.650(1) Å and the shorter average N−O bond length of 1.207(2) Å found in complex **1**, compared to the average Fe−N bond distance of 1.637(3) Å and average N−O bond length of 1.223(3) Å found in $[PPN]_2[Fe_2(\mu\text{-}S^tBu)_2(NO)_4]$,[40] are consistent with a relatively

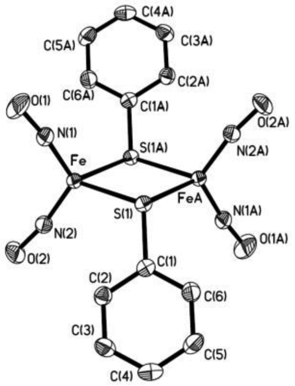

Figure 1. ORTEP drawing and labeling scheme of the $[Fe_2(\mu\text{-}SPh)_2(NO)_4]^{2-}$ unit in PPh_4 salt (**1**) with thermal ellipsoids drawn at 50% probability. Selected bond distances (Å) and angles (deg): Fe···FeA 3.613 (3); Fe−N(1) 1.6464(14); Fe−N(2) 1.6534(14); Fe−S(1) 2.3623(4); Fe−S(1A) 2.3678(4); N(1)−O(1) 1.2038(18); N(2)−O(2) 1.2097(17); N(1)−Fe−N(2) 117.73(7); N(1)−Fe−S(1) 111.49(5); N(2)−Fe−S(1) 114.15(5); N(1)−Fe−S(1A) 114.44(5); N(2)−Fe−S(1A) 112.97(5); S(1) −Fe−S(1A) 80.403(3); O(1)−N(1)−Fe 172.45(14); O(2)−N(2)−Fe 166.97(13); Fe−S(1)−Fe(1A) 99.596(16).

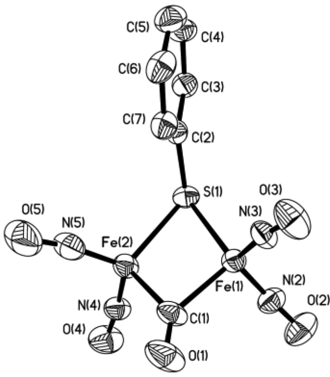

Figure 2. ORTEP drawing and labeling scheme of $[Fe(NO)_2(\mu\text{-}SPh)(\mu\text{-}CO)Fe(NO)_2]^-$ unit in PPh_4 salt (**2**) with thermal ellipsoids draw at 50% probability. Selected bond distances (Å) and angles (deg): Fe(1)···Fe(2) 2.5969(8); Fe(1)−N(2) 1.660(4); Fe(1)−N(3) 1.655(4); Fe(2)−N(4) 1.650(4); Fe(2)−N(5) 1.646(4); Fe(1)−S(1) 2.2734(11); Fe(2)−S(1) 2.2803(11); Fe(1)−C(1) 1.936(4); Fe(2)−C(1) 1.948(4); O(2)−N(2) 1.177(4); O(3)−N(3) 1.178(4); O(4)−N(4) 1.179(4); O(5)−N(5) 1.182(4); C(1)−O(1) 1.165(3); N(2)−Fe(1)−N(3) 120.60(16); N(2)−Fe(1)−S(1) 109.12(12); N(3)−Fe(1)−S(1) 114.96(12); N(2)−Fe(1)−C(1) 103.74(17); N(3)−Fe(1)−C(1) 102.71(16); S(1)−Fe(1)−C(1)103.27(12); O(2)−N(2)−Fe(1) 171.9(3); O(3)−N(3)−Fe(1) 173.0(3) ; O(4)−N(4)−Fe(2) 171.1(3) ; O(5)−N(5)−Fe(2) 171.9(3).

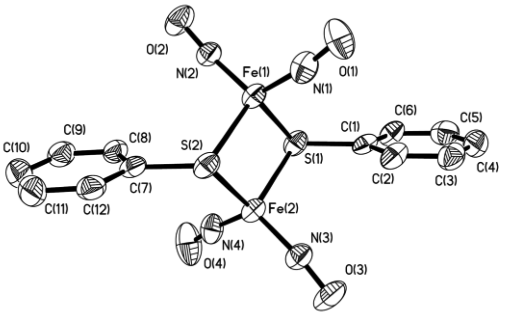

Figure 3. ORTEP drawing and labeling scheme of $[Fe_2(\mu\text{-}SPh)_2(NO)_4]^-$ (**3**) unit in PPh_4^+ salt (**3**) with thermal ellipsoids draw at 50% probability. Selected bond distances (Å) and angles (deg): Fe(1)···Fe(2) 2.8480(10); Fe(1)−N(1) 1.665(5); Fe(1)−N(2) 1.670(4); Fe(2)−N(3) 1.669(4); Fe(2)−N(4) 1.656(5); Fe(1)−S(1) 2.3120(15); Fe(1)−S(2) 2.3102(15); Fe(2)−S(1) 2.2999(15); Fe(2)−S(2) 2.3197(14); O(1)−N(1) 1.178(5); O(2)−N(2) 1.177(5); O(3)−N(3) 1.195(5); O(4)−N(4) 1.184(6); N(1)−Fe(1)−N(1) 117.7(2); N(1)−Fe(1)−S(1) 107.71(16); N(1)−Fe(1)−S(2) 107.30(18); N(2)−Fe(1)−S(1) 110.05(15); N(2)−Fe(1)−S(2) 109.27(15); S(1)−Fe(1)−S(2)103.86(5); O(1)−N(1)−Fe(1) 171.0(5); O(2)−N(2)−Fe(1) 170.2(4) ; O(3)−N(3)−Fe(2) 167.8(4) ; O(4)−N(4)−Fe(2) 172.5(4).

considerable degree of π back-bonding in the $\{Fe(NO)_2\}^{10}$ core induced by the distinct electron donating ability of phenyl-thiolate and alkyl−thiolate ligands.

As shown in Table 1, the average Fe−S bond lengths of 2.365(1), 2.310(2), and 2.260(1) Å in complexes **1**, **3**, and **4**, respectively, indicate that oxidation occurs from the antibonding orbitals of Fe−S bond. This is accompanied by the increase of average Fe−N(O) bond length from 1.650(1) to 1.665(4) Å and to 1.676(1)Å and the decrease of average N−O bond length from 1.207(1) to 1.184(5) Å and to 1.165(2) Å for complex **1**-to-**3**-to-**4**. In comparison with the average Fe−S bond length of 2.365(1) Å, the Fe−N(O) bond length of 1.650(1) Å and the N−O bond length of 1.207(2) Å for $\{Fe(NO)_2\}^{10}$-$\{Fe(NO)_2\}^{10}$ complex **1**, $\{Fe(NO)_2\}^{10}$-$\{Fe(NO)_2\}^{10}$ complex **2** shows the average Fe−S bond length of 2.277(1) Å, the N−O bond length of 1.179(4) Å and Fe−N(O) bond length of 1.653(4) Å. Complexes **1**−**4** display the distinct Fe···Fe distances, 3.613(2) Å for $\{Fe(NO)_2\}^{10}$-$\{Fe(NO)_2\}^{10}$ complex **1**, 2.848(1) Å for $\{Fe(NO)_2\}^{10}$-$\{Fe(NO)_2\}^{9}$ complex **3**, and 2.693(1) Å for $\{Fe(NO)_2\}^{10}$-$\{Fe(NO)_2\}^{9}$ complex **4**. Compared to complexes **3** and **4**, the Fe···Fe distance of complex **1** is lengthened to relieve the electronic richness for the stability of complex **1**. In contrast, $\{Fe(NO)_2\}^{10}$-$\{Fe(NO)_2\}^{10}$ complex **2** is stabilized by relieving the electronic richness of $\{Fe(NO)_2\}^{10}$-$\{Fe(NO)_2\}^{10}$ core via the strong π-accepting bridging CO.

Table 1. Selected Metric Data for Complexes 1−4

	1	2	3	4
Fe···Fe (Å)	3.613(2)	2.597(1)	2.848(1)	2.693(1)
Fe−S (Å)^a	2.365(1)	2.277(1)	2.310(2)	2.260(1)
Fe−N (Å)^a	1.650(1)	1.653(4)	1.665(4)	1.676(1)
N−O (Å)^a	1.207(2)	1.179(4)	1.184(5)	1.165(2)
S···S (Å)	3.053(2)		3.639(2)	3.631(1)
Fe−S−Fe ∠(deg)	99.6(1)	69.5(1)	76.1(1)^a	73.14(1)
Fe−C−Fe ∠(deg)		83.92(15)		
S−Fe−S ∠(deg)	80.4(1)		103.9(1)^a	106.9(1)
S−Fe−C ∠(deg)		103.27(12)^a		
N−Fe−N ∠(deg)^a	117.7(1)	120.3(2)^a	118.4(2)	117.4(1)
Fe−N−O ∠(deg)^a	169.7(1)^a	171.9(3)^a	170.4(4)^a	169.95(1)^a
dihedral ∠(deg)^b	180	172	180	180

^{a}Average bond distance and angle. ^{b}Defined by the intersection of two $[Fe_2S]$ planes.

Fe K-Edge Absorption Spectroscopy. The Fe K-edge X-ray absorption spectra of a series of dinuclear $\{Fe(NO)_2\}^{9/10}$-$\{Fe(NO)_2\}^{9/10}$ DNICs (complexes **1**−**4**) are depicted in Figure 4 and Table 2. The pre-edge 1s → 3d transitions, due to the d−p mixing between Fe and ligand atoms in the distorted T_d local environment of the Fe center, are enlarged in the inset to clarify the differences among these complexes. It has been known that the pre-edge energy is correlated with the oxidation state of

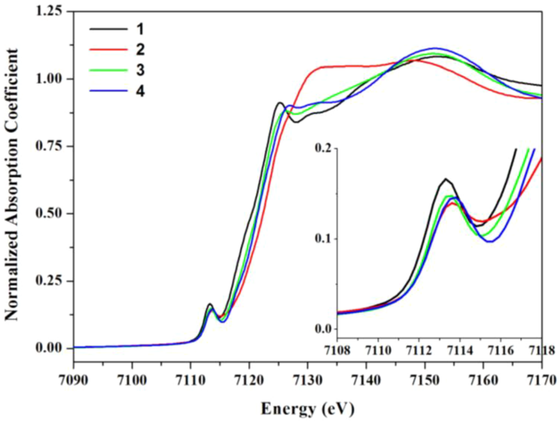

Figure 4. Fe K-edge absorption spectra of complexes **1**−**4**. (inset) The pre-edge absorption spectra.

Table 2. Pre-Edge Energy of Complexes 1−4 Derived from Fe K-Edge XAS

complexes	pre-edge energy (eV)
$[PPh_4]_2[Fe_2(\mu\text{-}SPh)_2(NO)_4]$ (**1**)	7113.3
$[PPh_4][Fe_2(\mu\text{-}SPh)(\mu\text{-}CO)(NO)_4]$ (**2**)	7113.6
$[PPh_4][Fe_2(\mu\text{-}SPh)_2(NO)_4]$ (**3**)	7113.5
$[Fe_2(\mu\text{-}SPh)_2(NO)_4]$ (**4**)	7113.8

metal containing the same coordination ligand environment and geometry.[45] In the Fe K-edge XAS, the pre-edge energies of the dinuclear DNIC redox complexes **1**, **3**, and **4** with the similar coordination geometries could be adopted to mark the oxidation states of the Fe center.[45,46] Obviously, the apparent pre-edge energy of Fe K-edge XAS shifted from 7113.3 and 7113.5 eV for complexes **1** and **3**, respectively, to 7113.8 eV for complex **4** indicates the higher effective nuclear charge (Z_{eff}) and oxidation state of Fe in complex **4** upon two-electron oxidation of the $\{Fe(NO)_2\}^{10}$-$\{Fe(NO)_2\}^{10}$ complex **1**, consistent with the trend on those of another structurally analogous dinuclear DNIC redox complexes $[Fe_2(\mu\text{-}S^tBu)_2(NO)_4]^{2-/1-/0}$.[40] It is interesting to note that the pre-edge energy of 7113.6 eV for complex **2** ($\{Fe(NO)_2\}^{10}$-$\{Fe(NO)_2\}^{10}$ core) is higher than that of complex **1** (7113.3 eV) but lies between 7113.5 eV (complex **3** with $\{Fe(NO)_2\}^{10}$-$\{Fe(NO)_2\}^{9}$ core) and 7113.8 eV (complex **4** with $\{Fe(NO)_2\}^{9}\{Fe(NO)_2\}^{9}$ core). This result indicates that the Fe K-edge pre-edge peak position of dinuclear DNICs is obviously perturbed by not only metal oxidation state and coordination geometry but also the ligand environment.[28] As the spectrometer energy resolution (0.15 at 708 eV) in Fe $L_{III,II}$-edge (2p → 3d transitions) is better than that of Fe K-edge, the Fe $L_{III,II}$-edge absorption were also measured, as shown in SI Figure S3. The results indicate that the similar trend as that of Fe K-edge pre-edge results by using the apparent peak energy for comparisons among complexes **1**, **3**, and **4**. In general, the multiplet effects of crystal field should be calculated to interpret the Fe $L_{III,II}$-edge spectrum well. Since the ligands and local geometry of complexes **1**, **3**, and **4** are the same, the apparent peak position is helpful in elucidating the electronic structures of $\{Fe(NO)_2\}$ core of complexes **1**, **3**, and **4**. In addition, the evaluation of the electronic richness of Fe center in complexes **1**−**4** by the characteristic pre-edge energy of Fe K-edge XAS is consistent with the conclusion from the intensity-weighted IR ν_{NO} stretching frequencies. It is noticed that the higher IR ν_{NO} stretching frequencies from complex **1** to **3** to **4** could reflect the variation in the electronic richness of $\{Fe(NO)_2\}$ core, as observed in the pre-edge energies of Fe K-edge XAS increasing from complex **1** (7113.3 eV) to complex **3** (7113.5 eV) and to complex **4** (7113.8 eV) (Figure 5).

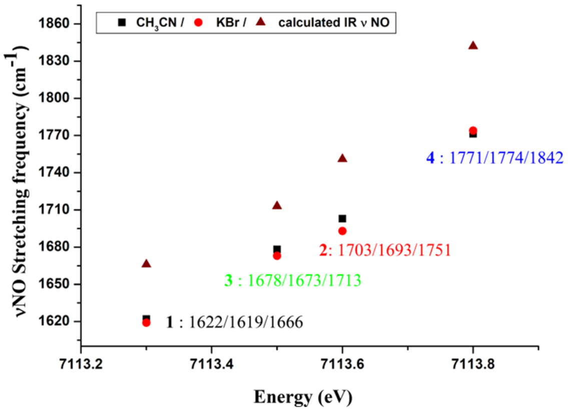

Figure 5. Plot of experimental and calculated intensity-weighted IR ν_{NO} stretching frequencies and Fe K-edge pre-edge energies of complexes **1**−**4**.

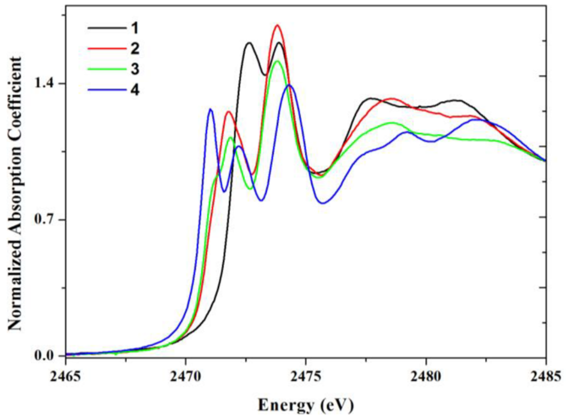

Figure 6. S K-edge absorption spectra of complexes **1**−**4**.

S K-Edge Absorption Spectroscopy. The S K-edge X-ray absorption spectra of complexes **1**−**4** are depicted in Figure 6, and the corresponding pre-edge energies and thiolate peak energies are collected in Table 3. In comparison with the intense $S_{1s} \rightarrow S_{C-S}\ \sigma^*$ transition of free $[SPh]^-$ at 2472.9 eV, the higher thioate peak energies of complexes **1**−**4** at 2473.8, 2473.8, 2473.8, and 2474.3 eV, respectively, imply the obvious charge dispersion from bridging-thiolate ligand to the $\{Fe(NO)_2\}$ cores of dinuclear DNICs. The same $S_{1s} \rightarrow S_{C-S}\ \sigma^*$ transition energies of complexes **1** and **3** reveal that complexes **1** and **3** exhibit the similar Z_{eff} of sulfur,[43] in contrast to complex **4** showing the higher Z_{eff} of sulfur. In the pre-edge region of S K-edge XAS derived from the $S_{1s} \rightarrow Fe_{3d}$ transition, complex **1** shows one pre-edge absorption peak at 2472.6 eV. The absorption peak shifts to 2471.3 (shoulder) and 2471.9 eV upon one-electron oxidation of complex **1** to afford complex **3**. However, one-electron oxidation of complex **3** yielding complex **4** displayed two well-resolved absorption peaks at 2471.0 and 2472.2 eV. As shown in Figure 6, a pre-edge absorption peak at 2471.8 eV can be observed for complex **2**, but no absorption peak at lower energy of ~2471.0 eV.

The previous studies have concluded that the relative energy of the S_{1s} orbital of [M−S] complexes (M = Fe and Ni) could be calculated from the $S_{1s} \rightarrow S_{C-S}\ \sigma^*$ transition energies.[47−51] Consequently, the pre-edge energies of $S_{1s} \rightarrow Fe_{3d}$ transition may be used to estimate the relative energy of the Fe_{3d} manifold orbitals and the effective nuclear charge Z_{eff} of the Fe center in MNICs and DNICs.[52−55] The relative Fe_{3d} manifold orbital energies of complexes **1**−**4** are calculated by setting the reference energy levels on $[Fe^{III}(SPh)_4]^-$, as shown in the previous study,[43] and listed in Table 3. As shown in Table 3, the Fe_{3d} manifold orbital energies of complexes **1**, **2**, and **3** are estimated to be 1.8, 1.0, and 1.1 eV, respectively, higher than that of complex **4** (0.3 eV). The decreasing relative d-manifold energy from **1** to **3** to **4** implicates that one-electron oxidation may increase the Z_{eff} of Fe to induce the increasing shift of 0.7−0.8 eV. This trend is consistent with the increasing pre-edge energies of Fe K-edge XAS from 7113.3 to 7113.5 eV to 7113.8 eV upon going from **1** to **3** to **4**, respectively. However, the variations obtained from the pre-edge peak of Fe K-edge XAS are smaller than those from the S K-edge XAS.

Table 3. Pre-Edge Energy, Thiolate Peak Energy, and the Calculated Relative d-Manifold Energy Shift Derived from S K-Edge XAS

complexes	pre-edge energy (eV)[a]	averaged thiolate pre-edge energy (eV)[b]	thiolate peak energy (eV)[a]	relative d-manifold energy shift (eV)[c]	oxidation state of Fe	Z_{eff} of Fe
$[Fe^{II}(SPh)_4]^{2-}$ [d]	2471.4	2471.4	2473.3	1.1	2.0	6.25
$[Fe^{III}(SPh)_4]^{-}$ [d]	2470.2	2470.2	2473.2	0	3.0	6.60
$[PPh_4][(SPh)_2Fe(NO)_2]$	(2470.6 2471.3)	2471.0	2473.5	0.5	2.59	6.46
1	2472.6	2472.6	2473.8	1.8	1.48	6.07
2	2471.8	2471.8	2473.8	1	2.17	6.31
3	(2471.3 2471.9)	2471.9	2473.8	1.1	2.08	6.28
4	(2471.0 2472.2)	2471.6	2474.3	0.3	2.75	6.51

[a] The pre-edge and thiolate peak energies are determined by the minimum of the second derivative. [b] The intensity-weighted average energy is given here. [c] Calculated from the difference of the thiolate peak energy and the intensity-weighted pre-edge peak energy. [d] From refs 52−55.

The reason may be due to the apparent peak position is used to assigned as 1s→ 3d transitions. As a matter of fact, the best way to describe the pre-edge transitions is to deconvolute the peak based on the crystal field multiplet calculations.[45] In addition, the slightly lower Fe_{3d} manifold orbital energy of complex **2**, compared with that of complex **3**, reveals that the Z_{eff} of Fe in complex **2** is slightly higher than that of complex **3**, consistent with the trend probed by Fe pre-edge K-edge energies and IR ν_{NO} stretching frequencies. In comparison with $\{Fe(NO)_2\}^{10}$-$\{Fe(NO)_2\}^{10}$ cores of complexes **1** and **2**, the significant lower Fe_{3d} manifold orbital energy of complex **2** indicates that the Z_{eff} of Fe in complex **2** is definitely higher than that of complex **1**. On the basis of the linear relationship between the oxidation state and the Z_{eff},[43,55] the Z_{eff} of Fe in $[(SPh)_2Fe(NO)_2]^-$, **1**, **2**, **3**, and **4** are estimated as 6.46, 6.07, 6.31, 6.28, and 6.51, respectively, and the corresponding oxidation states are 2.59, 1.48, 2.17, 2.08, and 2.75, respectively, when the oxidation states of $[Fe^{II}(SPh)_4]^{2-}$ and $[Fe^{III}(SPh)_4]^{-}$ are defined as 2.0 and 3.0, respectively. Detailed information is listed in Table 3. These results indicate that the average oxidation state of Fe of complex **1** is closer to Fe^{II}, and the oxidation state of Fe is close to Fe^{III} in complex **4**.

N K-Edge Absorption Spectroscopy. In addition to Fe and S K-edge XAS, N K-edge XAS was also employed to explore the electronic structure of the $\{Fe(NO)_2\}$ cores and characterize the property of NO ligand in complexes **1**−**4**. The N K-edge absorption spectra of complexes **1**−**4** are displayed in Figure 7. In general, the apparent peak in the range of 398−401 eV is derived from the $N_{1s} \rightarrow \pi^*$ transition, and the broad peak around 413 eV is mainly derived from the transition of $N_{1s} \rightarrow \sigma^*(NO)$.[56,57] By using the minimum of second derivative of absorption spectrum around 413 eV, the transition energies of $N_{1s} \rightarrow \sigma^*$ are determined as ~412.2 eV, ~412.5 eV, ~412.3 eV, and ~412.6 eV for complexes **1**, **2**, **3**, and **4**, respectively. In combination of Fe/S K-edge XAS and the similar $N_{1s} \rightarrow \pi^*$ transition energy from complex **1** to **3** to **4**, we assume the π orbital contributions of NO are almost the same among these complexes. We may conclude that the higher IR ν_{NO} stretching frequencies are associated with higher transition energy of $N_{1s} \rightarrow \sigma^*(NO)$ as shown in Figure 8a. Also, the higher transition energy of $N_{1s} \rightarrow \sigma^*(NO)$ is accompanied by the shorter N−O bond distances from complex **1** to **3** to **4**, that is, in the order of

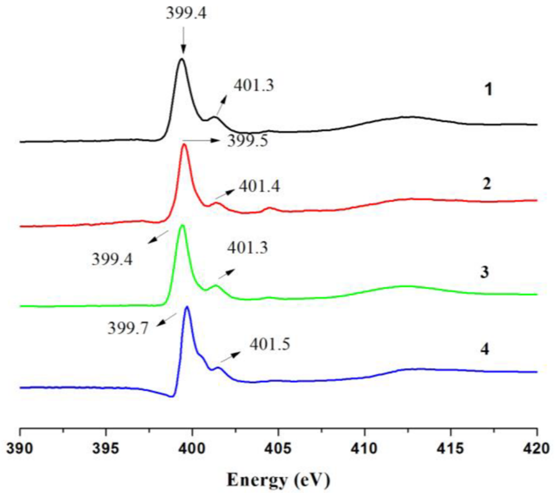

Figure 7. N K-edge absorption spectra of complexes **1**−**4**.

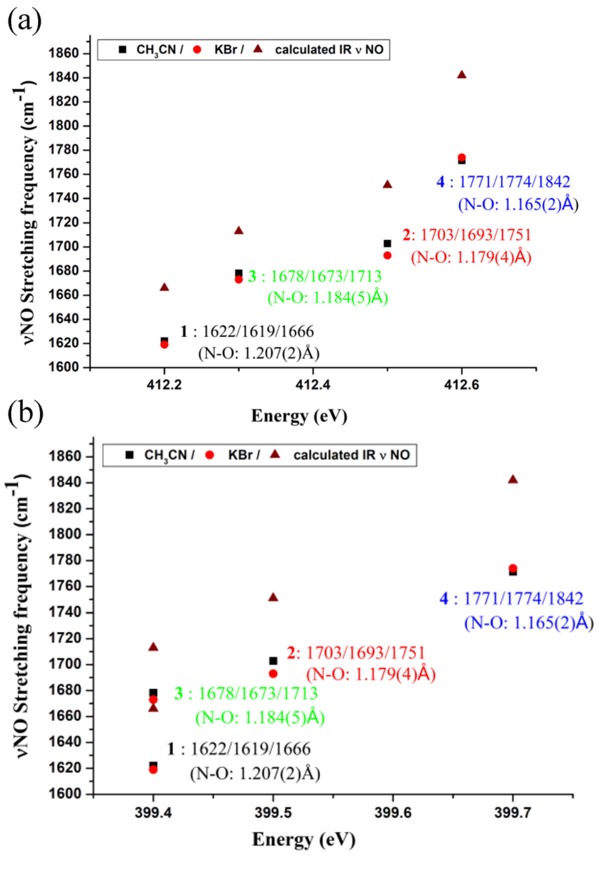

Figure 8. Plot of experimental and calculated intensity-weighted IR ν_{NO} stretching frequencies and N K-edge energies of complexes **1**−**4**. (a) $N_{1s} \rightarrow \sigma^*$, (b) $N_{1s} \rightarrow \pi^*$.

Table 4. Fe/N K-Edge Energies, NO Bond Length, and IRν_{NO} of Complexes 1−4

complexes	Fe pre-edge energy (eV)	N K-edge energy (eV) N 1s→σ^* (N 1s→π^*)	IRν_{NO} stretching frequency (cm^{-1})	N−O distance (average) (Å)
1	7113.3	412.2 (399.4)	1646, 1611, 1603	1.207(2)
2	7113.6	412.5 (399.5)	1702, 1685	1.179(4)
3	7113.5	412.3 (399.4)	1680, 1665	1.184(5)
4	7113.8	412.6 (399.7)	1702, 1685	1.165(2)

complex **1** (1.207(2) Å) > complex **3** (1.184(5) Å) > complex **2** (1.179(4) Å) > complex **4** (1.165(2) Å).

As shown in Figure 7, complex **1** demonstrates a strong transition peak of $N_{1s} \rightarrow \pi^*$ at 399.4 eV. Surprisingly, the N K-edge absorption spectrum of complex **3** shows the same $N_{1s} \rightarrow \pi^*$ transition energy upon one-electron oxidation of complex **1** yielding complex **3**. In contrast, the strong absorption peak at 399.4 eV of complex **3** shifts to 399.7 eV with a shoulder at 400.4 eV upon one-electron oxidation of complex **3** yielding complex **4**. From comparisons of $N_{1s} \rightarrow \pi^*$ transition energy among complexes **1**, **3**, and **4**, the lower $N_{1s} \rightarrow \pi^*$ energy of complex **3**, in contrast to that of complex **4**, indicates that one-electron oxidation of complex **1** to complex **3** seems to have no influence on the N atom of complex **1**, but it does have some effect on the N atom from oxidation of complex **3** yielding complex **4**; but this effect is not so large. The correlation between IR ν_{NO} stretching frequencies and $N_{1s} \rightarrow \pi^*$ transition energy was also displayed in Figure 8b. On the basis of the variations of bond lengths among Fe−S, Fe−N, and N−O in all complexes, the highest occupied molecular orbital (HOMO) should include the contributions of π bonding between Fe(3d) and π^*(NO) orbitals. Since the increase of Fe−N bond lengths is accompanied by the decrease of N−O bond lengths from **1** to **3** to **4**, the trend of $N_{1s} \rightarrow \pi^*$ transition energy is definitely changed due to the contributions of Fe(3d) and π^*(NO) orbitals. When π^*(NO) is significantly dominated, compared to the contributions of Fe transition orbitals, the decrease of $N_{1s} \rightarrow \pi^*$ transition energy is associated with the increase of N−O bond lengths and the decrease of IR vibrational frequency of NO. Presumably, the one-electron oxidation of complex **1** yielding complex **3** mainly occurs on Fe site due to no significant differences on $S_{1s} \rightarrow S_{C-S}\ \sigma^*$, $N_{1s} \rightarrow \pi^*$, and $N_{1s} \rightarrow \sigma^*$ energies between complex **1** (2473.8, 399.4, and 412.2 eV, respectively) and complex **3** (2473.8, 399.4, and 412.3 eV, respectively) (Tables 3 and 4).The further one-electron oxidation of complex **3** yielding complex **4** occurs at S, NO, and Fe site, and induces the less NO$^-$ character in complex **4**, reflecting the shift of 0.3 eV ($N_{1s} \rightarrow \pi^*$) and decrease of NO bond length ~0.02 Å (Tables 1 and 4). In addition, the shift to a slightly higher energy of the $N_{1s} \rightarrow \pi^*$ transition in complex **2** may be rationalized by the less electron back-donation from Fe atom to NO molecule due to the replacement of one bridged π-donor thiolate ligand with the strong π-acceptor carbonyl ligand. All detailed discussions will be made in terms of MO and time-dependent density functional theory (TD-DFT) calculations.

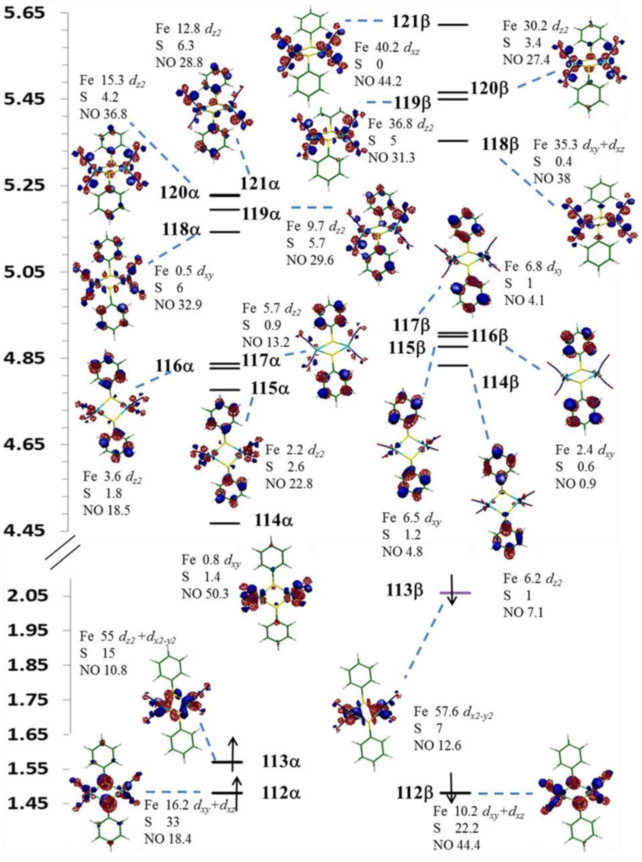

Figure 9. MO energy diagram of complex **1**. The numbers shown after Fe/S/NO in percentages are the major contribution of orbitals Fe(3d), NO(2p), and S(3p) in each MO.

MO and TD-DFT Calculations. The MO diagrams of complexes **1**, **2**, **3**, and **4** were depicted in Figure 9 and SI Figures S6, S4, and S5, respectively. In comparisons with MO diagrams of $[(NO)_2Fe(\mu\text{-SEt})]_2^z$ (z = 0, −1) and $[(NO)_2Fe(\mu\text{-S}^t\text{Bu})]_2^z$ (z = 0, −1, −2),[37,40] all of complexes display the similar character on chemical bonding. The highest occupied MO 113α/β of complex **1** is the hybridization of Fe($d_{x^2-y^2}$/d_{z^2}), S(3p), and NO(2p), which is dominated by the contributions of the antibonding character between Fe(d) and Fe(d), Fe(d) and S atoms, and bonding character between Fe(d) and π^*(NO) group. The lowest unoccupied orbital 114α is related to the antibonding character between Fe(d_{xy}) and π^*(NO) group, but dominated by the contribution of π^*(NO) group. This rationalizes the decrease of Fe−S/N−O bond distances and the increase of Fe−N bond lengths from $\{Fe(NO)_2\}^{10}$-$\{Fe(NO)_2\}^{10}$ of complex **1** to $\{Fe(NO)_2\}^{10}$-$\{Fe(NO)_2\}^9$ of complex **3**, and to $\{Fe(NO)_2\}^9$-$\{Fe(NO)_2\}^9$ of complex **4** (Table 1). When one electron is removed from the highest occupied 113β in complex **1** to form complex **3**, the pre-edge peak of Fe K-edge XAS (complex **3**) shifts to higher energy, which indicates the increasing of Z_{eff} at Fe site, so that the 3d orbitals shift to lower energy as shown in the natural bonding orbital (NBO) analysis of SI Figure S7. The similar variation is also observed in oxidation of complex **1** to **3** (Table 3). This is due to the dominated contribution of Fe(3d) orbitals in HOMO of complexes **1** and **3**. That is, the bonding characters of Fe−S and Fe···Fe are enhanced. Moreover, the NBO analysis indicates that the oxidation state of each Fe is changed from +2 to +2.5 to +3 from complex **1** to **3** to **4**, and both $\{Fe(NO)_2\}^9$ cores are in antiferromagnetic coupling fashion in complex **4**, whose spin density is displayed in SI Figure S8. This trend is consistent with the oxidation states derived from S K-edge analysis. The electronic structures of complexes **1**, **3**, and **4** displayed quite similar character as reported by Yeh et al.,[40] where four of five 3d orbitals in high-spin Fe(III) are strongly π-bonding with NO. The last 3d-based orbital may act as the electron acceptor orbital upon reduction of $\{Fe(NO)_2\}^9$ yielding $\{Fe(NO)_2\}^{10}$.[58]

The TD-DFT calculation on the pre-edge transitions of S K-edge XAS and the comparison with experimental results were displayed in Figure 10 and SI Figures S9–S10 for complex **1**, **3**, and **4**, respectively.[40,43,55,59−61] On the basis of the results of TD-DFT calculations, the peaks observed at 2471.3 and 2471.0 eV for complexes **3** and **4**, respectively, are corresponding to the transition of S_{1s} to the unoccupied MO, mainly contributed from the Fe($d_{x^2-y^2}$) and S(3p) orbitals (113β and 113α/β shown in SI Figures S9 and S10, respectively). The absorption peak at 2472.6 eV for complex **1** and the second absorption peak at 2471.9 eV for complex **3** (2472.2 eV for complex **4**) were associated with the transitions from S_{1s} to unoccupied MOs related to Fe–S antibonding and to the antibonding orbital dominated by the contributions of S, NO(π^*), and Fe(d) orbitals (MO 114α/β-117α/β shown in Figure 10 and SI Figures S9 and S10). The absorption peak at ~2471.8 eV in complex **2** is assigned as the transition $S_{1s} \rightarrow$ MO 92. In comparison with the MO diagrams of complexes **3** and **4**, displayed in SI Figures S4 and S5, removing one electron at occupied 113α in complex **3** is accompanied by creating another unoccupied orbital dominated by Fe($d_{x^2-y^2}$) and S(3p) (i.e., unoccupied 113α and 113β in complex **4**; 47.5% Fe($d_{x^2-y^2}$) + 15.5% S(3p) + 6.6% NO), so that the intensity of pre-edge peak is increased upon oxidation of complex **3** yielding **4**. It rationalizes the significant variation in S K-edge pre-edge spectra. Moreover, because of the decreasing bonding character of Fe–N(O) and antibonding character of N–O going from complex **3** to complex **4**, it is expected that the Fe–N bonding is weakened and N–O bonding is enhanced.

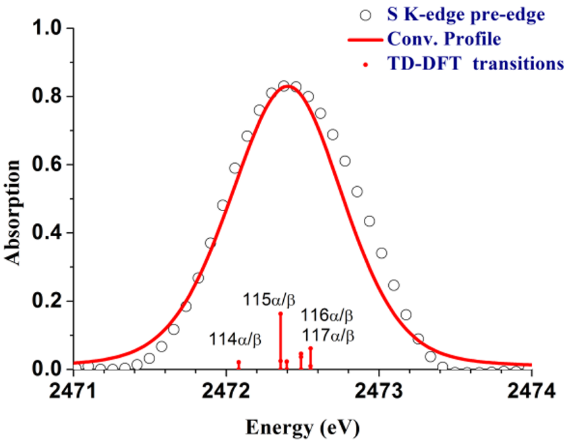

Figure 10. Experimental (○) and TD-DFT-calculated (red solid line) of S K-edge pre-edge absorption of complex **1**. The vertical lines are theoretically calculated peaks. The calculated transitions are convoluted with a pseudo-Voigt function (Lorentzian (L)/Gaussian-(G) = 1/1) and with a 0.36 eV half-width to account for experiment and core-hole broadening. A further transition energy shifted by 46.6 eV is applied to get better agreement between the experimental and the calculated profile.

The TD-DFT calculation of $N_{1s} \rightarrow \pi^*$ transition energies and the comparison with experimental results are shown in Figure 11 and SI Figures S11 and S12 for complex **1**, **3**, and **4**, respectively. The major contribution of this absorption peak is mainly the transition to 114α, which is mainly the contribution of ~50% NO in complex **1**. This indicates that the $N_{1s} \rightarrow \pi^*$ absorption peak is related to the N–O antibonding character. When oxidation occurred from complex **1** to complex **3** by removing one electron at 113β, the contribution of NO(π^*) in unoccupied 113β is too small (~4.8%) so that we observe the same $N_{1s} \rightarrow \pi^*$ transition energies of complexes **3** and **1**. In examining the $N_{1s} \rightarrow \pi^*$ transitions of complex **3** oxidized to form **4**, the major contribution is to excite one electron to the orbitals of 114α/β and even with higher energy, which is significantly dominated by NO(π^*). However, due to the rearrangement of NO(π^*) and Fe(d_{xy}) contributions in 114β (from 17.8% to 58.2% for NO(π^*) ; from 42% to 17.9% for Fe(d_{xy})), it will affect $N_{1s} \rightarrow \pi^*$ transition shift to higher energy by 0.3 eV so that the associated IR stretching frequencies also shift to higher frequencies were observed.

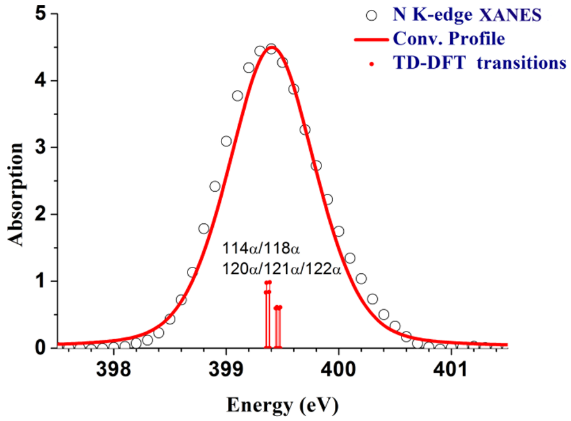

Figure 11. Experimental (○) and TD-DFT-calculated (red solid line) of N K-edge $N_{1s} \rightarrow \pi^*$ absorption of complex **1**. The vertical lines are theoretically calculated peaks. The calculated transitions are convoluted with a pseudo-Voigt function (L/G = 1/1) and with a 0.4 eV half-width to account for experiment and core-hole broadening. A further transition energy shifted by 13.2 eV is applied to get better agreement between the experimental and the calculated profile.

The $\{Fe(NO)_2\}^{10}$-$\{Fe(NO)_2\}^{10}$ complex **2** containing a carbonyl-bridged ligand was employed to elucidate the distinct electronic effect on the Fe atom and NO ligand of $\{Fe(NO)_2\}$ moiety when one of the phenylthiolate-bridged ligands of complex **1** was replaced by a σ donor and π acceptor CO ligand. Such bonding effect can be illustrated in the HOMO−1 (MO 90) shown in Figure 12, which is a hybridization with ~19% Fe ($d_{x^2-y^2}$), ~17% CO, ~11% S, and ~25.6% NO. This MO elucidates the back-donation of Fe($d_{x^2-y^2}$) to π acceptor CO ligand, so that Z_{eff} of Fe in complex **2** is higher than that in complex **1**.

■ CONCLUSION AND COMMENTS

Studies on the syntheses, N/S/Fe K-edge XAS, and DFT computation of the direduced-form RRE **1**, reduced-form RRE **3**, RRE **4**, and mixed-CO-thiolate-bridged direduced-form RRE **2** have resulted in the following conclusions.

1. For the synthetic methodology: (a) In contrast to the direduced-form RREs obtained from reduction of

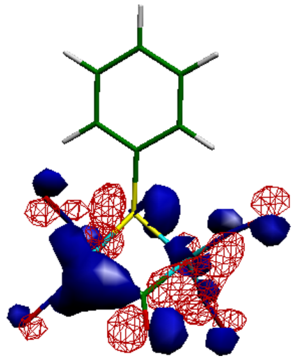

Figure 12. HOMO−1 of complex **2**.

thiolate-/phenolate-bound $\{Fe(NO)_2\}^9$ DNICs, the successful synthesis of complex **1** provides the new synthetic pathway for the syntheses of direduced-form RREs. (b) The transformation of complex **1** to complex **3** via complex **2** may provide an alternative route for the syntheses of $\{Fe(NO)_2\}^9$-$\{Fe(NO)_2\}^{10}$ reduced-form RREs, in contrast to reduced-form RREs derived from reduction of $\{Fe(NO)_2\}^9$-$\{Fe(NO)_2\}^9$ neutral RREs uncovered in the previous study.

2. The MO energy diagram of complex **1** indicates that the HOMO ($113\alpha/\beta$) is a linear combination with Fe($d_{x^2-y^2}$)/Fe(d_{z^2}), S(p_x) and NO(p_z), which is mainly contributed from the antibonding character between Fe(d) and Fe(d), Fe(d) and S atoms, and bonding character between Fe(d) and NO(π^*). That is, the consecutive oxidation from complex **1** to **3** and then from **3** to **4** enhances bonding character of Fe−S and N−O bonds, but weakens bonding character of Fe−N bonds. It rationalizes that the N−O and Fe−S bond lengths of complexes **1**, **3**, and **4** are in the order of complex **1** > complex **3** > complex **4**; in contrast, the Fe−N bond distances are in the order of complex **4** > complex **3** > complex **1**, as shown in Table 1.
3. As HOMO is dominated by the contribution of Fe(d) for complexes **1**, **3**, and **4**, removing electrons from HOMO definitely increases the effective nuclear charge (Z_{eff}) of Fe site. It explains pre-edge energy of Fe shifts from 7113.3 eV for complex **1** to 7113.5 eV for complex **3** and then to 7113.8 eV for complex **4** (Table 2).
4. On the basis of the experimental IR ν_{NO} stretching frequencies and XANES of Fe/S/N K-edge energies shown in Tables 2−4 and Figures 5 and 8, we demonstrate that the Fe/S K-edge pre-edge energy and N K-edge XAS can be employed to delineate N−O bonding character in the dinuclear DNICs system. The lower IR ν_{NO} stretching frequencies and the longer N−O bond lengths are associated with the lower transition energy of $N_{1s} \rightarrow \sigma^*$(NO), that is, the $N_{1s} \rightarrow \sigma^*$(NO) transition energies (412.2, 412.3, and 412.6 eV) of complexes **1**, **3**, and **4**, respectively, reflect the ν_{NO} stretching frequencies as (1646, 1611, 1603 cm^{-1} for **1**), (1680, 1665 cm^{-1} for **3**), and (1761, 1720 cm^{-1} for **4**), and the N−O bond distances of complexes **1**, **3**, and **4** are in the order of complex **1** (1.207(2) Å) > complex **3** (1.184(5) Å) > complex **4** (1.165(2) Å) (Table 4). Moreover, on the basis of S K-edge pre-edge energy, the relative d-manifold energy of Fe is in the order of complex **1** > complex **3** > complex **4**, which is consistent with the Z_{eff} of Fe site (complex **1** < complex **3** < complex **4**). This also explains the average bond lengths of Fe−S are in the order of complex **1** (2.365(1) Å) > complex **3** (2.310(2) Å) > complex **4** (2.260(1) Å).
5. On the basis of N/S/Fe K-edge XAS, oxidation mainly occurs at Fe site when complex **1** is oxidized to form complex **3**; in contrast, oxidation of complex **3** yielding complex **4** occurs at Fe, S, and NO.
6. In complex **2**, the strong π-acceptor CO-coordinated ligand bridged to $Fe(NO)_2\}^{10}$-$\{Fe(NO)_2\}^{10}$ motif significantly modulates the bonding character between Fe and S/NO due to the increasing Z_{eff} of Fe site, as observed in IR ν_{NO} stretching frequencies and Fe/N/S K-edge XAS.

■ EXPERIMENTAL SECTION

Manipulations, reactions, and transfers were conducted under nitrogen according to Schlenk techniques or in a glovebox (nitrogen gas). Solvents were distilled under nitrogen from appropriate drying agents (methylene chloride from CaH_2; acetonitrile from CaH_2−P_2O_5; diethyl ether, hexane, and tetrahydrofuran (THF) from sodium benzophenone) and stored in dried, N_2-filled flasks over 4 Å molecular sieves. Nitrogen was purged through these solvents before use. Solvent was transferred to the reaction vessel via stainless cannula under positive pressure of N_2. The reagents, tetraphenylphosphonium bromide ([PPh_4][Br]), iron pentacarbonyl (Strem), *N,N,N′,N′*-tetramethylethylenediamine (TMEDA), nitrosonium tetrafluoroborate (Alfa Aesar), and diphenyl disulfide (Acros) were used as received. [PPN][$Fe(CO)_3(NO)$] and [Fe(TMEDA)$(NO)_2$] were prepared according to the literature procedure.[62,63] Infrared spectra of the carbonyl ν(CO) and the nitrosyl ν(NO) stretching frequencies were recorded on Bruker ALPHA FTIR spectrophotometer or Thermo FTIR Nicolet iS5/iD1 spectrophotometer with sealed solution cells (0.1 mm, KBr/CaF_2 windows) or KBr disc. UV−vis spectra were recorded on a Thermo Evolution 201 UV−vis spectrophotometer. Cyclic voltammetry (CV) was carried out with a CH Instruments electrochemical analyzer 611C. A three-electrode system consisted of a glassy carbon working electrode, a platinum wire auxiliary electrode, and a 0.1 M Ag/Ag$^+$ reference electrode. CV data was recorded with the scan rate of 0.5 V s^{-1} in CH_3CN with tetrabutylammonium hexafluorophosphate as the supporting electrolyte. All potential values are reported verseus ferrocene/ferrocenium ion. ^{1}H NMR spectra were obtained on a Varian AC 400 spectrometer. Elemental analyses of carbon, hydrogen, and nitrogen were obtained with a Heraeus CHN−O−S Rapid Analyzer.

Preparation of [PPh_4]$_2$[$Fe_2(\mu$-SPh$)_2(NO)_4$] (1). Fifteen milliliters of THF was added to the 20 mL Schlenk tube loaded with [Fe(TMEDA)$(NO)_2$] (0.464 g, 2.0 mmol) and [PPh_4][SPh] (0.900 g, 2.0 mmol). After the reaction mixture was stirred overnight at ambient temperature under N_2 atmosphere, the resulting suspensions were stood to afford the yellow-green precipitates. When the upper THF solution was removed by cannula under positive N_2 atmosphere, the yellow-green precipitates were washed by THF twice and dried under vacuum to afford [PPh_4]$_2$[$Fe_2(\mu$-SPh$)_2(NO)_4$] (**1**) (yield: 0.905 g, 80.2%). The dark-green crystals suitable for single-crystal X-ray diffraction were afforded by storing the green CH_3CN solution of complex **1** at −15 °C for two weeks. IR: 1646 (s), 1611 (s), 1603 (s) (ν_{NO}) cm^{-1} (KBr); 1644 (s), 1604 (s) (ν_{NO}) cm^{-1} (CH_3CN). Absorption spectrum (CH_3CN) [$\lambda_{\max}$, nm (ϵ, M^{-1} cm^{-1})]: 365 (10154), 460 (4182), 641 (2471), 984 (2736). Anal. Calcd for $C_{60}H_{50}Fe_2N_4O_4P_2S_2$: C, 63.84; H, 4.46; N, 4.96. Found: C, 63.13; H, 4.15; N, 4.64%.

Preparation of [PPh_4][$Fe_2(\mu$-SPh$)(\mu$-CO$)(NO)_4$] (2). The THF solution (15 mL) of 0.5 mmol $Fe(CO)_2(NO)_2$, prepared fleshly from reaction of [NO][BF_4] (0.059 g, 0.5 mmol) and [PPN][Fe-$(CO)_3(NO)$] (0.354 g, 0.5 mmol) in THF, was transferred to a 50 mL Schlenk flask loaded with [PPh_4]$_2$[$Fe_2(\mu$-SPh$)_2(NO)_4$] (**1**) (0.226 g, 0.2 mmol) by cannula under positive pressure of N_2 at ambient temperature. After the reaction mixture was stirred overnight, the reaction solution was monitored by FTIR. The IR spectrum showing the ν_{NO} stretching bands at 1846 (w) (ν_{CO}), 1706 (s), and 1694 (s) cm^{-1}(ν_{NO}) (THF) was assigned to the formation of $[PPh_4][Fe_2(\mu\text{-}SPh)(\mu\text{-}CO)(NO)_4]$ (**2**). When the reaction solution was filtered through Celite to remove the insoluble solids, the blue filtrate was concentrated to 5 mL under vacuum, and 35 mL of diethyl ether was added to precipitate the blue solids of complex **2** (yield: 0.253 g, 89.4%). The dark blue crystals suitable for X-ray crystallography were afforded by laying the blue THF solution of complex **2** with hexane at −15 °C for 10 d. IR: 1846 (w) (ν_{CO}), 1706 (s), 1694 (s) (ν_{NO}) cm^{-1} (THF); 1843 (w) (ν_{CO}), 1709 (s), 1697 (s) (ν_{NO}) cm^{-1} (CH_3CN); 1825 (w) (ν_{CO}), 1702 (s), 1685 (s) (ν_{NO}) cm^{-1} (KBr). Absorption spectrum (THF) [λ_{max}, nm (ϵ, M^{-1} cm^{-1})]: 364 (5935), 616 (2493), 969 (607). Anal. Calcd for $C_{31}H_{25}Fe_2N_4O_5PS$: C, 52.57; H, 3.56; N, 7.91. Found: C, 52.60; H, 3.53; N, 7.46%.

Preparation of $[PPh_4][Fe_2(\mu\text{-}SPh)_2(NO)_4]$ (3). Complex **2** (0.142 g, 0.2 mmol) and $(PhS)_2$ (0.044 g, 0.2 mmol) were loaded in a 50 mL Schlenk flask, and then 15 mL of THF was added to the Schlenk flask. After the reaction solution was stirred at ambient temperature overnight, the reaction solution was monitored by FTIR. The IR spectrum showing the ν_{NO} stretching bands at 1688 (s) and 1667 (vs) cm^{-1}(ν_{NO}) (THF) was assigned to the formation of $[PPh_4][Fe_2(\mu\text{-}SPh)(NO)_4]$ (**3**). When the reaction solution was filtered through Celite to remove the insoluble solids, the green filtrate was concentrated to 5 mL under vacuum, and 35 mL of diethyl ether was added to precipitate the blue solids of complex **3** (yield: 0.126 g, 79.6%). The green THF solution of complex **3** was layered with hexane at −15 °C for 5 d to afford dark green crystals suitable for X-ray crystallography. IR ν_{NO}: 1688 (s), 1667 (s) cm^{-1} (THF); 1688 (s), 1671 (s) cm^{-1} (CH_3CN); 1680 (s), 1665 (s) cm^{-1} (KBr). Absorption spectrum (CH_3CN) [λ_{max}, nm (ϵ, M^{-1} cm^{-1})]: 367 (13619), 459 (5811), 651 (2922), 985 (3696)]. Anal. Calcd for $C_{36}H_{30}Fe_2N_4O_4PS_2$: C, 54.77; H, 3.83; N, 7.10. Found: C, 54.65; H, 3.72; N, 6.99%.

Preparation of $[Fe_2(\mu\text{-}SPh)_2(NO)_4]$ (4). $(PhS)_2$ (0.044 g, 0.2 mmol) and $[(TMEDA)Fe(NO)_2]$ (0.092 g, 0.4 mmol) were loaded in a 20 mL Schlenk tube and dissolved in 10 mL of THF. After the reaction mixture was stirred for 48 h, the reaction solution was monitored by FTIR. The IR spectrum showed three stretching bands at 1814 (w), 1783 (s), and 1757 (s) cm^{-1}(ν_{NO}) (THF) and was assigned to the formation of $[Fe_2(\mu\text{-}SPh)_2(NO)_4]$ (**4**). The reaction solution was filtered through Celite, and then the filtrate was dried under vacuum leading to the dark brown solids. After the dark brown solids were washed with 8 mL of hexane, the dark brown solids of complex **4** were afforded (yield 0.064 g, 71.2%). IR ν_{NO}: 1814 (w), 1783 (s), 1757 (s) cm^{-1} (THF); 1817 (w), 1786 (s), 1759 (s) cm^{-1} (CH_3CN); 1761 (s), 1720 (s) cm^{-1} (KBr). Anal. Calcd for $C_{12}H_{10}Fe_2N_4O_4S_2$: C, 32.02; H, 2.24; N, 12.45. Found: C, 33.04; H, 2.74; N, 11.42%.

Reaction of $[PPh_4]_2[Fe_2(\mu\text{-}SPh)_2(NO)_4]_2$ (1) with 1 equiv of $[Fe_2(\mu\text{-}SPh)_2(NO)_4]_2$ (4). A THF solution of complex **4** (0.090 g, 0.2 mmol) was transferred to a 20 mL Schlenk tube loaded with complex **1** (0.226 g, 0.2 mmol) by a cannula under positive N_2 pressure at ambient temperature. The reaction was stirred for 24 h under nitrogen at ambient temperature and monitored by FTIR. The IR spectrum showing two absorption bands at 1688 (s) and 1667 (vs) cm^{-1} (THF) implied the formation of $[PPh_4][Fe_2(\mu\text{-}SPh)_2(NO)_4]_2$ (**3**). The green solution was filtered through Celite to remove insoluble solid. After the green filtrate was concentrated to 5 mL, hexane was added to precipitate the dark green solids of complex **3** (yield: 0.125 g, 79.4%).

Reaction of $[PPh_4][Fe_2(\mu\text{-}SPh)_2(NO)_4]$ (3) with 1 equiv of $Fe(CO)_2(NO)_2$. The THF solution (15 mL) of 0.3 mmol $Fe(CO)_2(NO)_2$, prepared fleshly from reaction of $[NO][BF_4]$ (0.036 g, 0.3 mmol) and $[PPN][Fe(CO)_3(NO)]$ (0.213 g, 0.3 mmol) in THF, was transferred to a 50 mL Schlenk flask loaded with $[PPh_4][Fe_2(\mu\text{-}SPh)_2(NO)_4]$ (**3**) (0.158 g, 0.2 mmol) by cannula under positive pressure of N_2 at ambient temperature. After the reaction solution was stirred for 3 h, the reaction mixture was filtered through Celite to remove the insoluble solids. When the blue filtrate was dried under vacuum, 30 mL of diethyl ether was added to separate product $[PPh_4][Fe_2(\mu\text{-}SPh)(\mu\text{-}CO)(NO)_4]$ (**2**) (diethyl ether insoluble) and $[Fe_2(\mu\text{-}SPh)_2(NO)_4]$ (**4**) (diethyl ether soluble). After drying insoluble dark-blue solids of complex **2** and diethyl ether solution of complex **4** separately under vacuum, 0.115 g of dark blue solids of complex **2** (yield 81.3%) and 0.038 g of dark brown solids of complex **4** (yield 84.4%) were afforded.

EPR Measurement. EPR measurement was performed at X-band using a Bruker EMX spectrometer equipped with Bruker TE 102 cavity. The microwave frequency was measured with a Hewlett-Packard 5246L electronic counter. At 298 K, X-band EPR spectrum of complex **3** in THF was obtained with a microwave power of 19.97 mW, frequency at 9.4852 GHz, and modulation amplitude of 0.8 G at 100 kHz.

X-ray Absorption Measurements. All X-ray absorption experiments were carried out at the National Synchrotron Radiation Research Center (NSRRC), Hsinchu, Taiwan. The Fe K-edge absorption spectra were measured in transmission mode at the BL-17 C wriggler beamline with a double-crystal Si(111) monochromator (DCM). The energy resolution $\Delta E/E$ is ~2.2×10^{-4}. The associated spectrometer energy resolution is 0.32 at 7112 eV. The step size over the edge region is 0.3 eV, and the reproducibility in energy determination is <0.2 eV, as determined from repeated calibration and sample measurements during separate experimental runs. High harmonics were rejected by using Rh-coated mirrors. The spectra were scanned from 6.912 to 7.972 keV using a gas-ionization detector under ambient conditions. A reference Fe foil was always measured simultaneously, and the first inflection point at 7112.0 eV was used for energy calibration. The background subtraction and normalization of Fe K-edge spectra were done by the AUTOBK program.[64]

For Fe L-edge measurements, the data were collected at the BL20A high-energy spherical grating monochromator (HSGM) beamline with 10 μm opening slits, corresponding to 0.15 eV energy resolution for the Fe L-edge energy range. All samples were ground to powder from single crystals, stuck to a conducting tape, and then put into an ultrahigh vacuum chamber (10^{-9} Torr). The spectra were recorded in the electron-yield mode and with a microchannel plate (MCP) as the detector. Each spectrum was calibrated by using the known Fe L_{III} edge absorption peak at 708.5 eV of Fe_2O_3.

All S K-edge XAS experiments were obtained at BL-16A with a Si(111) DCM. The energy resolution $\Delta E/E$ was ~1.4×10^{-4}. The spectra were taken in fluorescence mode with a Lytle detector, and the sample chamber was filled with high-purity He gas to avoid air absorption. The photon energy is calibrated from the S K-edge spectra of $Na_2S_2O_3 \cdot 5H_2O$ and assigns the maximum of the first pre-edge peak to 2472.02 eV. The sample was ground from single crystal into powder before use. The spectrum is measured from 2.42 to 2.772 keV. The monochromator step size over the edge region is 0.08 eV. The spectra were reduced and normalized based on the procedures reported by Solomon et al. The pre-edge features at the S K-edge were fitted using the methods described in our previous results.

The spectra of N K-edge absorption were collected at BL-20A with slit of 20 × 20 μm. Samples were prepared as mentioned above, stuck to a conducting tape, and loaded into a vacuum chamber (10^{-9} Torr). The spectra were taken in total electron yield mode. Energy was calibrated against nitrogen at 401 eV of BN absorption. The backgrounds of the spectra were removed by fitting a straight line to the pre-edge region and subtracting this straight line from the entire spectra. The reproducibility in energy determination is ~0.1 eV, which is determined from repeated calibration and sample measurements during different experimental runs. To compare the results of different complexes, we estimate the standard deviation of energy is 0.1 eV.

Molecular Orbitals Calculation. All molecular orbital (MO) and time-dependent density functional theory (TD-DFT) calculations for S and N K-edge regions were performed on the ORCA package version 3.0.2.[65] The relativistic effect by zeroth order regular approximation (ZORA) is included in all calculations. The coordinates used for geometry optimization of complexes **1**−**4** were based on the experimental structures taken from the X-ray diffraction experiments.[38,66] The coordinate system employed is such that the origin is set as the center between two Fe atoms; the *x*-axis is collinear with the

Fe(1)−Fe(2) direction; the *y*-axis is perpendicular to *x*-axis and in the direction of center to S(1). The B3LYP* exchange functional with the def2-TZVP(-f) basis set on the Fe, S, N, O, C, and H atoms were used in the geometry optimization. Broken symmetry method was used to obtain the ground state in all compounds. In complex **2**, as the overlap between α and β orbitals in MO91 (HOMO) is close to one (0.9667), we present a closed shell calculation result. There are only very small imaginary frequencies at approximately -12 and -35 cm^{-1}, and the corresponding intensity is zero in complexes **3** and **4**; no imaginary frequency appears in complexes **1** and **2**. How the different exchange functionals influence the TD-DFT results on S/N K-edge pre-edge regions are tested, and the better one is to mix ∼15% Hartree_Fock exchange (HFx) for compromised all of complexes. Thus, we apply the B3LYP* functional on all electronic calculations. Complexes **1**, **2**, and **4** were calculated at closed-shell level due to the diamagnetism, but complex **3** was done at unrestricted open-shell level. The MO and TD-DFT calculation were done at the same exchange functional and def2-TZVP(-f) basis set. The LÖwdin population analysis was used to obtain the contributions of Fe, S, and NO on each MO. Isosurface plots of the MOs were generated using the Molekel program version 4.3 with an isovalue surface at 0.04 au.

Crystallography. Crystallographic data and structure refinements parameters of complexes **1**−**3** are summarized in the Supporting Information (Tables S1−S3). The crystals of complexes **1**, **2**, and **3** chosen for X-ray diffraction studies are measured in sizes of 0.40 × 0.25 × 0.25 mm, 0.30 × 0.25 × 0.03 mm, and 0.30 × 0.15 × 0.15 mm, respectively. Each crystal was mounted on a glass fiber and quickly coated in epoxy resin. Unit-cell parameters were obtained by least-squares refinement. Diffraction measurements for complexes **1**, **2**, and **3** were carried out on a Nonius Kappa CCD and Bruker SMART Apex CCD diffractometers using graphite-monochromated Mo Kα radiation (λ = 0.7107 Å) and between 1.87 and 27.50° for complex **1**, between 1.34 and 27.49° for complex **2**, and between 0.94 and 27.50° for complex **3**. Least-squares refinement of the positional and anisotropic thermal parameters for the contribution of all non-hydrogen atoms and fixed hydrogen atoms was based on F^2. A SADABS absorption correction was made.[67] The SHELXTL structure refinement program was employed.[68]

ASSOCIATED CONTENT

Supporting Information

X-ray crystallographic files in CIF format for structure determinations of $[\mathrm{PPh_4}]_2[\mathrm{Fe_2}(\mu\text{-SPh})_2(\mathrm{NO})_4]$ (**1**), $[\mathrm{PPh_4}][\mathrm{Fe_2}(\mu\text{-SPh})(\mu\text{-CO})(\mathrm{NO})_4]$ (**2**), and $[\mathrm{PPh_4}][\mathrm{Fe_2}(\mu\text{-SPh})_2(\mathrm{NO})_4]$ (**3**). Cyclic voltammogram of complex **1**, EPR spectrum of complex **3**, MO energy diagram of complex **3**, Fe $\mathrm{L_{III,II}}$-edge spectra of complexes **1**−**4**, NBO analysis of d-orbital population, spin-density distribution of complex **4**, experimental and TD-DFT-calculated K-edge spectra of complexes **2**, **3**, and **4**, tabulated crystallographic data and structure refinement for complexes **1**, **2**, and **3**. This material is available free of charge via the Internet at http://pubs.acs.org.

AUTHOR INFORMATION

Corresponding Authors

*E-mail: cchwind@csmu.edu.tw. (C.-H.C.)
*E-mail: ijuihsu@ntut.edu.tw. (I.-J.H.)

Notes

The authors declare no competing financial interest.

ACKNOWLEDGMENTS

We gratefully acknowledge financial support from the Ministry of Science and Technology (Taiwan). Authors thank Mr. G.-H. Lee for single-crystal X-ray structural determinations. We also thank Dr. S.-W. Yeh, Dr. J.-F. Lee, L.-Y. Jang, J.-M. Chen, J.-M. Lee, and National Synchrotron Radiation Research Center of Taiwan (NSRRC) for their support on the hardware and software applied in this work.

REFERENCES

(1) Furchgott, R. F.; Vanhoutte, P. M. *FASEB J.* **1989**, *3*, 2007−2018.

(2) Ignarro, L. J.; Buga, G. M.; Wood, K. S.; Byrns, R. E.; Chaudhuri, G. *Proc. Natl. Acad. Sci. U. S. A.* **1987**, *84*, 9265−9269.

(3) Rapoport, R. M.; Draznin, M. B.; Murad, F. *Nature* **1983**, *306*, 174−176.

(4) Prast, H.; Philippu, A. *Prog. Neurobiol.* **2001**, *64*, 51−68.

(5) MacMicking, J.; Xie, Q. W.; Nathan, C. *Annu. Rev. Immunol.* **1997**, *15*, 323−350.

(6) Ignarro, L. J. *Annu. Rev. Pharmacol. Toxicol.* **1990**, *30*, 535−560.

(7) Butler, A. R.; Megson, I. L. *Chem. Rev.* **2002**, *102*, 1155−1165.

(8) Hayton, T. W.; Legzdins, P.; Sharp, W. B. *Chem. Rev.* **2002**, *102*, 935−991.

(9) Vahtras, O.; Almloef, J.; Feyereisen, M. W. *Chem. Phys. Lett.* **1993**, *213*, 514−18.

(10) McCleverty, J. A. *Chem. Rev.* **2004**, *104*, 403−418.

(11) Boese, M.; Mordvintcev, P. I.; Vanin, A. F.; Busse, R.; Mulsch, A. *J. Biol. Chem.* **1995**, *270*, 29244−29249.

(12) Henry, Y.; Lepoivre, M.; Drapier, J. C.; Ducrocq, C.; Boucher, J. L.; Guissani, A. *FASEB J.* **1993**, *7*, 1124−1134.

(13) Mulsch, A.; Mordvintcev, P.; Vanin, A. F.; Busse, R. *FEBS Lett.* **1991**, *294*, 252−256.

(14) Wiegant, F. A. C.; Malyshev, I. Y.; Kleschyov, A. L.; Van Faassend, E.; Vanin, A. F. *FEBS Lett.* **1999**, *455*, 179−182.

(15) Cooper, C. E. *Biochim. Biophys. Acta, Bioenerg.* **1999**, *1411*, 290−309.

(16) Foster, M. W.; Cowan, J. A. *J. Am. Chem. Soc.* **1999**, *121*, 4093−4100.

(17) Cesareo, E.; Parker, L. J.; Pedersen, J. Z.; Nuccetelli, M.; Mazzetti, A. P.; Pastore, A.; Federici, G.; Caccuri, A. M.; Ricci, G.; Adams, J. J.; Parker, M. W.; Lo Bello, M. *J. Biol. Chem.* **2005**, *280*, 42172−42180.

(18) De Maria, F.; Pedersen, J. Z.; Caccuri, A. M.; Antonini, G.; Turella, P.; Stella, L.; Lo Bello, M.; Federici, G.; Ricci, G. *J. Biol. Chem.* **2003**, *278*, 42283−42293.

(19) Lancaster, J. R., Jr.; Hibbs, J. B., Jr. *Proc. Natl. Acad. Sci. U. S. A.* **1990**, *87*, 1223−7.

(20) Watts, R. N.; Hawkins, C.; Ponka, P.; Richardson, D. R. *Proc. Natl. Acad. Sci. U. S. A.* **2006**, *103*, 7670−7675.

(21) D'Autreaux, B.; Horner, O.; Oddou, J. L.; Jeandey, C.; Gambarelli, S.; Berthomieu, C.; Latour, J. M.; Michaud-Soret, I. *J. Am. Chem. Soc.* **2004**, *126*, 6005−6016.

(22) Ding, H. G.; Demple, B. *Proc. Natl. Acad. Sci. U. S. A.* **2000**, *97*, 5146−5150.

(23) Lee, M. H.; Arosio, P.; Cozzi, A.; Chasteen, N. D. *Biochemistry* **1994**, *33*, 3679−3687.

(24) Turella, P.; Pedersen, J. Z.; Caccuri, A. M.; De Maria, F.; Mastroberardino, P.; Lo Bello, M.; Federici, G.; Ricci, G. *J. Biol. Chem.* **2003**, *278*, 42294−42299.

(25) Chen, C.-H.; Chiou, S.-J.; Chen, H.-Y. *Inorg. Chem.* **2010**, *49*, 2023−2025.

(26) Hsieh, C. H.; Brothers, S. M.; Reibenspies, J. H.; Hall, M. B.; Popescu, C. V.; Darensbourg, M. Y. *Inorg. Chem.* **2013**, *52*, 2119−2124.

(27) Huang, H.-W.; Tsou, C.-C.; Kuo, T.-S.; Liaw, W.-F. *Inorg. Chem.* **2008**, *47*, 2196−2204.

(28) Tsai, M.-C.; Tsai, F.-T.; Lu, T.-T.; Tsai, M.-L.; Wei, Y.-C.; Hsu, I. J.; Lee, J.-F.; Liaw, W.-F. *Inorg. Chem.* **2009**, *48*, 9579−9591.

(29) Tsai, M.-L.; Hsieh, C.-H.; Liaw, W.-F. *Inorg. Chem.* **2007**, *46*, 5110−5117.

(30) Reginato, N.; McCrory, C. T. C.; Pervitsky, D.; Li, L. J. *J. Am. Chem. Soc.* **1999**, *121*, 10217−10218.

(31) Wang, J.-H.; Chen, C.-H. *Inorg. Chem.* **2010**, *49*, 7644−7646.

(32) Wang, R.; Wang, X.; Sundberg, E. B.; Nguyen, P.; Grant, G. P. G.; Sheth, C.; Zhao, Q.; Herron, S.; Kantardjieff, K. A.; Li, L. *Inorg. Chem.* **2009**, *48*, 9779−9785.

(33) Tinberg, C. E.; Tonzetich, Z. J.; Wang, H.; Do, L. H.; Yoda, Y.; Cramer, S. P.; Lippard, S. J. *J. Am. Chem. Soc.* **2010**, *132*, 18168−18176.

(34) Crack, J. C.; Smith, L. J.; Stapleton, M. R.; Peck, J.; Watmough, N. J.; Buttner, M. J.; Buxton, R. S.; Green, J.; Oganesyan, V. S.; Thomson, A. J.; Le Brun, N. E. *J. Am. Chem. Soc.* **2011**, *133*, 1112−1121.

(35) Cruz-Ramos, H.; Crack, J.; Wu, G. G.; Hughes, M. N.; Scott, C.; Thomson, A. J.; Green, J.; Poole, R. K. *EMBO J.* **2002**, *21*, 3235−3244.

(36) Pullan, S. T.; Gidley, M. D.; Jones, R. A.; Barrett, J.; Stevanin, T. M.; Read, R. C.; Green, J.; Poole, R. K. *J. Bacteriol.* **2007**, *189*, 1845−1855.

(37) Lu, T.-T.; Tsou, C.-C.; Huang, H.-W.; Hsu, I. J.; Chen, J.-M.; Kuo, T.-S.; Wang, Y.; Liaw, W.-F. *Inorg. Chem.* **2008**, *47*, 6040−6050.

(38) Tsou, C.-C.; Lu, T.-T.; Liaw, W.-F. *J. Am. Chem. Soc.* **2007**, *129*, 12626−12627.

(39) Wang, R.; Camacho-Fernandez, M. A.; Xu, W.; Zhang, J.; Li, L. *Dalton Trans.* **2009**, 777−786.

(40) Yeh, S.-W.; Lin, C.-W.; Li, Y.-W.; Hsu, I. J.; Chen, C.-H.; Jang, L.-Y.; Lee, J.-F.; Liaw, W.-F. *Inorg. Chem.* **2012**, *51*, 4076−4087.

(41) Lu, C.-Y.; Liaw, W.-F. *Inorg. Chem.* **2013**, *52*, 13918−13926.

(42) Tonzetich, Z. J.; Wang, H.; Mitra, D.; Tinberg, C. E.; Do, L. H.; Jenney, F. E., Jr.; Adams, M. W. W.; Cramer, S. P.; Lippard, S. J. *J. Am. Chem. Soc.* **2010**, *132*, 6914−6916.

(43) Lu, T.-T.; Lai, S.-H.; Li, Y.-W.; Hsu, I. J.; Jang, L.-Y.; Lee, J.-F.; Chen, I. C.; Liaw, W.-F. *Inorg. Chem.* **2011**, *50*, 5396−5406.

(44) Horrocks, W. D.; Taylor, R. C. *Inorg. Chem.* **1963**, *2*, 723−727.

(45) Westre, T. E.; Kennepohl, P.; DeWitt, J. G.; Hedman, B.; Hodgson, K. O.; Solomon, E. I. *J. Am. Chem. Soc.* **1997**, *119*, 6297−6314.

(46) DuBois, J. L.; Mukherjee, P.; Stack, T. D. P.; Hedman, B.; Solomon, E. I.; Hodgson, K. O. *J. Am. Chem. Soc.* **2000**, *122*, 5775−5787.

(47) Dey, A.; Chow, M.; Taniguchi, K.; Lugo-Mas, P.; Davin, S.; Maeda, M.; Kovacs, J. A.; Odaka, M.; Hodgson, K. O.; Hedman, B.; Solomon, E. I. *J. Am. Chem. Soc.* **2006**, *128*, 533−541.

(48) Dey, A.; Jeffrey, S. P.; Darensbourg, M.; Hodgson, K. O.; Hedman, B.; Solomon, E. I. *Inorg. Chem.* **2007**, *46*, 4989−4996.

(49) Lugo-Mas, P.; Dey, A.; Xu, L.; Davin, S. D.; Benedict, J.; Kaminsky, W.; Hodgson, K. O.; Hedman, B.; Solomon, E. I.; Kovacs, J. A. *J. Am. Chem. Soc.* **2006**, *128*, 11211−11221.

(50) Shearer, J.; Dehestani, A.; Abanda, F. *Inorg. Chem.* **2008**, *47*, 2649−2660.

(51) Szilagyi, R. K.; Bryngelson, P. A.; Maroney, M. J.; Hedman, B.; Hodgson, K. O.; Solomon, E. I. *J. Am. Chem. Soc.* **2004**, *126*, 3018−3019.

(52) Glaser, T.; Rose, K.; Shadle, S. E.; Hedman, B.; Hodgson, K. O.; Solomon, E. I. *J. Am. Chem. Soc.* **2001**, *123*, 442−454.

(53) Shadle, S. E.; Hedman, B.; Hodgson, K. O.; Solomon, E. I. *Inorg. Chem.* **1994**, *33*, 4235−4244.

(54) Shadle, S. E.; Hedman, B.; Hodgson, K. O.; Solomon, E. I. *J. Am. Chem. Soc.* **1995**, *117*, 2259−2272.

(55) Sun, N.; Liu, L. V.; Dey, A.; Villar-Acevedo, G.; Kovacs, J. A.; Darensbourg, M. Y.; Hodgson, K. O.; Hedman, B.; Solomon, E. I. *Inorg. Chem.* **2011**, *50*, 427−436.

(56) Nardi, M. V.; Detto, F.; Aversa, L.; Verucchi, R.; Salviati, G.; Iannotta, S.; Casarin, M. *Phys. Chem. Chem. Phys.* **2013**, *15*, 12864−12881.

(57) Shimada, T.; Kondoh, H.; Iwasaki, M.; Nakai, I.; Nagasaka, M.; Amemiya, K.; Orita, H.; Ohta, T. *J. Phys. Chem. B* **2006**, *110*, 20507−20512.

(58) Ye, S.; Neese, F. *J. Am. Chem. Soc.* **2010**, *132*, 3646−3647.

(59) DeBeer George, S.; Neese, F. *Inorg. Chem.* **2010**, *49*, 1849−1853.

(60) Lee, C.-R.; Hsu, I. J.; Chen, H.-T.; Lee, G.-H.; Wang, Y. *C. R. Chim.* **2012**, *15*, 237−249.

(61) Lee, Y.-W.; Hsu, I. J. *J. Chin. Chem. Soc.* **2013**, *60*, 935−941.

(62) Hedberg, L.; Hedberg, K.; Satija, S. K.; Swanson, B. I. *Inorg. Chem.* **1985**, *24*, 2766−2771.

(63) Hung, M.-C.; Tsai, M.-C.; Lee, G.-H.; Liaw, W.-F. *Inorg. Chem.* **2006**, *45*, 6041−6047.

(64) Frenkel, A.; Stern, E. A.; Voronel, A.; Qian, M.; Newville, M. *Phys. Rev. B* **1994**, *49*, 11662−11674.

(65) Neese, F. *ORCA - an ab initio, Density Functional and Semiempirical Program Package, 2.9.1*; University of Bonn, Germany, 2012.

(66) Harrop, T. C.; Song, D. T.; Lippard, S. J. *J. Am. Chem. Soc.* **2006**, *128*, 3528−3529.

(67) Sheldrick, G. M. *SADABS − A Software for Empirical Absorption Correction;* Bruker AXS: Madison, WI, 1997.

(68) Sheldrick, G. M. *SHELXTL: A Program for Crystal Structure Determination;* Bruker AXS: Madison, WI, 1994.